Fast and simple spectral FLIM for biochemical and medical imaging

Marina Popleteeva,[1] Kalina T. Haas,[1] David Stoppa,[2] Lucio Pancheri,[2,3] Leonardo Gasparini,[2] Clemens F. Kaminski,[4] Liam D. Cassidy,[1] Ashok R. Venkitaraman,[1,5] and Alessandro Esposito[1,5,*]

[1]*Medical Research Council Cancer Unit, University of Cambridge, Hutchison/MRC Research Centre, Box 197 Biomedical Campus, CB20XZ, Cambridge, UK*
[2]*Fondazione Bruno Kessler, Via Sommarive 18, 38123 Povo, Trento, Italy*
[3]*Department of Industrial Engineering, University of Trento, Via Mesiano 77, 38123 Trento, Italy*
[4]*Department of Chemical Engineering and Biotechnology, University of Cambridge, New Museums Site, Pembroke Street, CB23RA Cambridge, UK*
[5]*These joint senior authors contributed equally to this paper*
[*]*ae275@mrc-cu.cam.ac.uk*

Abstract: Spectrally resolved fluorescence lifetime imaging microscopy (λFLIM) has powerful potential for biochemical and medical imaging applications. However, long acquisition times, low spectral resolution and complexity of λFLIM often narrow its use to specialized laboratories. Therefore, we demonstrate here a simple spectral FLIM based on a solid-state detector array providing in-pixel histrogramming and delivering faster acquisition, larger dynamic range, and higher spectral elements than state-of-the-art λFLIM. We successfully apply this novel microscopy system to biochemical and medical imaging demonstrating that solid-state detectors are a key strategic technology to enable complex assays in biomedical laboratories and the clinic.

OCIS codes: (040.6070) Solid state detectors; (170.3880) Medical and biological imaging; (170.3650) Lifetime-based sensing; (110.4234) Multispectral and hyperspectral imaging.

References and links

1. N. Komatsu, K. Aoki, M. Yamada, H. Yukinaga, Y. Fujita, Y. Kamioka, and M. Matsuda, "Development of an optimized backbone of FRET biosensors for kinases and GTPases," Mol. Biol. Cell **22**(23), 4647–4656 (2011).
2. T. S. Blacker, Z. F. Mann, J. E. Gale, M. Ziegler, A. J. Bain, G. Szabadkai, and M. R. Duchen, "Separating NADH and NADPH fluorescence in live cells and tissues using FLIM," Nat. Commun. **5**, 3936 (2014).
3. F. Fereidouni, A. N. Bader, A. Colonna, and H. C. Gerritsen, "Phasor analysis of multiphoton spectral images distinguishes autofluorescence components of in vivo human skin," J. Biophotonics **7**(8), 589–596 (2014).
4. D. K. Bird, K. W. Eliceiri, C. H. Fan, and J. G. White, "Simultaneous two-photon spectral and lifetime fluorescence microscopy," Appl. Opt. **43**(27), 5173–5182 (2004).
5. Q. S. Hanley, D. J. Arndt-Jovin, and T. M. Jovin, "Spectrally resolved fluorescence lifetime imaging microscopy," Appl. Spectrosc. **56**(2), 155–166 (2002).
6. A. Rück, Ch. Hülshoff, I. Kinzler, W. Becker, and R. Steiner, "SLIM: a new method for molecular imaging," Microsc. Res. Tech. **70**(5), 485–492 (2007).
7. W. Becker, A. Bergmann, C. Biskup, T. Zimmer, N. Klocker, and K. Benndorf, "Multi-wavelength TCSPC lifetime imaging," Multiphoton Microsc. Biomed. Sci. II **4620**, 79–84 (2002).
8. S. R. Kantelhardt, J. Leppert, J. Krajewski, N. Petkus, E. Reusche, V. M. Tronnier, G. Hüttmann, and A. Giese, "Imaging of brain and brain tumor specimens by time-resolved multiphoton excitation microscopy ex vivo," Neuro-oncol. **9**(2), 103–112 (2007).
9. R. Patalay, C. Talbot, Y. Alexandrov, M. O. Lenz, S. Kumar, S. Warren, I. Munro, M. A. Neil, K. König, P. M. French, A. Chu, G. W. Stamp, and C. Dunsby, "Multiphoton multispectral fluorescence lifetime tomography for the evaluation of basal cell carcinomas," PLoS One **7**(9), e43460 (2012).
10. S. Schlachter, S. Schwedler, A. Esposito, G. S. Kaminski Schierle, G. D. Moggridge, and C. F. Kaminski, "A method to unmix multiple fluorophores in microscopy images with minimal a priori information," Opt. Express **17**(25), 22747–22760 (2009).
11. A. Esposito, M. Popleteeva, and A. R. Venkitaraman, "Maximizing the biochemical resolving power of fluorescence microscopy," PLoS One **8**(10), e77392 (2013).

#243323 Received 18 Jun 2015; revised 5 Aug 2015; accepted 5 Aug 2015; published 28 Aug 2015

12. F. Fereidouni, K. Reitsma, and H. C. Gerritsen, "High speed multispectral fluorescence lifetime imaging," Opt. Express **21**(10), 11769–11782 (2013).
13. W. Chen, E. Avezov, S. C. Schlachter, F. Gielen, R. F. Laine, H. P. Harding, F. Hollfelder, D. Ron, and C. F. Kaminski, "A method to quantify FRET stoichiometry with phasor plot analysis and acceptor lifetime ingrowth," Biophys. J. **108**(5), 999–1002 (2015).
14. W. Becker, A. Bergmann, G. Biscotti, K. König, I. Riemann, L. Kelbauskas, and C. Biskup, "High-speed FLIM data acquisition by time-correlated single photon counting," Proc. SPIE **5223**, 1–14 (2004).
15. W. Becker, *The bh TCSPC Handbook,* 6th ed. (Becker and Hicki, 2014).
16. D. McLoskey, D. J. S. Birch, A. Sanderson, K. Suhling, E. Welch, and P. J. Hicks, "Multiplexed single-photon counting. 1. A time-correlated fluorescence lifetime camera," Rev. Sci. Instrum. **67**(6), 2228–2237 (1996).
17. K. Suhling, D. McLoskey, and D. J. S. Birch, "Multiplexed single-photon counting.2. The statistical theory of time-correlated measurements," Rev. Sci. Instrum. **67**(6), 2238–2246 (1996).
18. L. Pancheri and D. Stoppa, "A SPAD-based pixel linear array for high-speed time-gated fluorescence lifetime imaging," 2009 P ESSCIRC, 429–432 (2009).
19. S. S. Kiwanuka, T. K. Laurila, J. H. Frank, A. Esposito, K. Blomberg von der Geest, L. Pancheri, D. Stoppa, and C. F. Kaminski, "Development of broadband cavity ring-down spectroscopy for biomedical diagnostics of liquid analytes," Anal. Chem. **84**(13), 5489–5493 (2012).
20. N. Krstajić, J. Levitt, S. Poland, S. Ameer-Beg, and R. Henderson, "256 × 2 SPAD line sensor for time resolved fluorescence spectroscopy," Opt. Express **23**(5), 5653–5669 (2015).
21. M. A. Digman, V. R. Caiolfa, M. Zamai, and E. Gratton, "The phasor approach to fluorescence lifetime imaging analysis," Biophys. J. **94**(2), L14–L16 (2008).
22. F. Fereidouni, A. Esposito, G. A. Blab, and H. C. Gerritsen, "A modified phasor approach for analyzing time-gated fluorescence lifetime images," J. Microsc. **244**(3), 248–258 (2011).
23. F. Fereidouni, A. N. Bader, and H. C. Gerritsen, "Spectral phasor analysis allows rapid and reliable unmixing of fluorescence microscopy spectral images," Opt. Express **20**(12), 12729–12741 (2012).
24. A. H. Clayton, Q. S. Hanley, and P. J. Verveer, "Graphical representation and multicomponent analysis of single-frequency fluorescence lifetime imaging microscopy data," J. Microsc. **213**(1), 1–5 (2004).
25. H. C. Gerritsen, M. A. Asselbergs, A. V. Agronskaia, and W. G. Van Sark, "Fluorescence lifetime imaging in scanning microscopes: acquisition speed, photon economy and lifetime resolution," J. Microsc. **206**(3), 218–224 (2002).
26. C. J. de Grauw and H. C. Gerritsen, "Multiple time-gate module for fluorescence lifetime imaging," Appl. Spectrosc. **55**(6), 670–678 (2001).
27. H. W. Ai, K. L. Hazelwood, M. W. Davidson, and R. E. Campbell, "Fluorescent protein FRET pairs for ratiometric imaging of dual biosensors," Nat. Methods **5**(5), 401–403 (2008).
28. A. Esposito, H. C. Gerritsen, F. S. Wouters, and U. Resch-Genger, "Fluorescence lifetime imaging microscopy: quality assessment and standards," in *Standardization in Fluorometry: State of the Art and Future Challenges*, O. S. Wolfbeis, ed. (Springer, Berlin Heidelberg New York, 2007).
29. F. Borghetti, D. Mosconi, L. Pancheri, and D. Stoppa, "CMOS single-photon avalanche diode sensor for fluorescence lifetime imaging," in *IEEE International Image Sensors Workshop*, 2007), 7–10.
30. HAMAMATSU, "Datasheet: Linear array multianode PMT and assembly R5900U-L16 series, H7260 series," (2003).
31. F. Fereidouni, G. A. Blab, and H. C. Gerritsen, "Blind unmixing of spectrally resolved lifetime images," J. Biomed. Opt. **18**(8), 086006 (2013).
32. M. Kollner and J. Wolfrum, "How many photons are necessary for fluorescence-lifetime measurements," Chem. Phys. Lett. **200**(1-2), 199–204 (1992).
33. A. Esposito, A. N. Bader, S. C. Schlachter, D. J. van den Heuvel, G. S. Schierle, A. R. Venkitaraman, C. F. Kaminski, and H. C. Gerritsen, "Design and application of a confocal microscope for spectrally resolved anisotropy imaging," Opt. Express **19**(3), 2546–2555 (2011).
34. W. R. Ware, S. K. Lee, G. J. Brant, and P. P. Chow, "Nanosecond time-resolved rmission rpectroscopy - spectral shifts due to solvent-excited solute relaxation," J. Chem. Phys. **54**(11), 4729–4737 (1971).
35. T. S. Forde and Q. S. Hanley, "Spectrally resolved frequency domain analysis of multi-fluorophore systems undergoing energy transfer," Appl. Spectrosc. **60**(12), 1442–1452 (2006).
36. J. A. Palero, H. S. de Bruijn, A. van der Ploeg-van den Heuvel, H. J. C. M. Sterenborg, and H. C. Gerritsen, "In vivo nonlinear spectral imaging in mouse skin," Opt. Express **14**(10), 4395–4402 (2006).
37. F. Skoulidis, L. D. Cassidy, V. Pisupati, J. G. Jonasson, H. Bjarnason, J. E. Eyfjord, F. A. Karreth, M. Lim, L. M. Barber, S. A. Clatworthy, S. E. Davies, K. P. Olive, D. A. Tuveson, and A. R. Venkitaraman, "Germline Brca2 heterozygosity promotes Kras(G12D) -driven carcinogenesis in a murine model of familial pancreatic cancer," Cancer Cell **18**(5), 499–509 (2010).
38. E. A. Jares-Erijman and T. M. Jovin, "FRET imaging," Nat. Biotechnol. **21**(11), 1387–1395 (2003).
39. J. M. Pavia, M. Wolf, and E. Charbon, "Measurement and modeling of microlenses fabricated on single-photon avalanche diode arrays for fill factor recovery," Opt. Express **22**(4), 4202–4213 (2014).
40. D. Bronzi, F. Villa, S. Bellisai, S. Tisa, A. Tosi, G. Ripamonti, F. Zappa, S. Weyers, D. Durini, W. Brockherde, and U. Paschen, "Large Area CMOS SPADs with very low dark counting rate," Quantum Sensing and Nanophotonic Devices **X**, 8631 (2013).

#243323 Received 18 Jun 2015; revised 5 Aug 2015; accepted 5 Aug 2015; published 28 Aug 2015

41. Q. S. Hanley and A. H. Clayton, "AB-plot assisted determination of fluorophore mixtures in a fluorescence lifetime microscope using spectra or quenchers," J. Microsc. **218**(1), 62–67 (2005).
42. Y. Niino, K. Hotta, and K. Oka, "Simultaneous live cell imaging using dual FRET sensors with a single excitation light," PLoS One **4**(6), e6036 (2009).
43. M. Zhao, R. Huang, and L. Peng, "Quantitative multi-color FRET measurements by Fourier lifetime excitation-emission matrix spectroscopy," Opt. Express **20**(24), 26806–26827 (2012).
44. D. M. Grant, W. Zhang, E. J. McGhee, T. D. Bunney, C. B. Talbot, S. Kumar, I. Munro, C. Dunsby, M. A. Neil, M. Katan, and P. M. French, "Multiplexed FRET to image multiple signaling events in live cells," Biophys. J. **95**(10), L69–L71 (2008).
45. D. M. Shcherbakova, M. A. Hink, L. Joosen, T. W. Gadella, and V. V. Verkhusha, "An orange fluorescent protein with a large Stokes shift for single-excitation multicolor FCCS and FRET imaging," J. Am. Chem. Soc. **134**(18), 7913–7923 (2012).
46. A. Esposito, H. C. Gerritsen, T. Oggier, F. Lustenberger, and F. S. Wouters, "Innovating lifetime microscopy: a compact and simple tool for life sciences, screening, and diagnostics," J. Biomed. Opt. **11**(3), 034016 (2006).
47. A. C. Mitchell, J. E. Wall, J. G. Murray, and C. G. Morgan, "Measurement of nanosecond time-resolved fluorescence with a directly gated interline CCD camera," J. Microsc. **206**(3), 233–238 (2002).
48. Q. Zhao, B. Schelen, R. Schouten, R. van den Oever, R. Leenen, H. van Kuijk, I. Peters, F. Polderdijk, J. Bosiers, M. Raspe, K. Jalink, J. Geert Sander de Jong, B. van Geest, K. Stoop, and I. T. Young, "Modulated electron-multiplied fluorescence lifetime imaging microscope: all-solid-state camera for fluorescence lifetime imaging," J. Biomed. Opt. **17**(12), 126020 (2012).
49. M. Gersbach, R. Trimananda, Y. Maruyama, M. Fishburn, D. Stoppa, J. Richardson, R. Walker, R. K. Henderson, and E. Charbon, "High frame-rate TCSPC-FLIM using a novel SPAD-based image sensor," Proc. SPIE **7780**, 77801H (2010).
50. D. D. U. Li, J. Arlt, D. Tyndall, R. Walker, J. Richardson, D. Stoppa, E. Charbon, and R. K. Henderson, "Video-rate fluorescence lifetime imaging camera with CMOS single-photon avalanche diode arrays and high-speed imaging algorithm," J. Biomed. Opt. **16**(9), 096012 (2011).
51. S. P. Poland, N. Krstajić, J. Monypenny, S. Coelho, D. Tyndall, R. J. Walker, V. Devauges, J. Richardson, N. Dutton, P. Barber, D. D. Li, K. Suhling, T. Ng, R. K. Henderson, and S. M. Ameer-Beg, "A high speed multifocal multiphoton fluorescence lifetime imaging microscope for live-cell FRET imaging," Biomed. Opt. Express **6**(2), 277–296 (2015).

1. Introduction

Fluorescence lifetime imaging microscopy (FLIM) enables cell biochemistry with the low invasiveness that is characteristic of fluorescence-based techniques either detecting exogenously expressed fluorescent sensors (*e.g.*, kinase or protease sensors) [1] or autofluorescence emitted by naturally occurring biomolecules, often generated by metabolism (*e.g.*, NADH and FAD) [2, 3]. Moreover, the combination of hyper-spectral detection and FLIM [4–7] has very high potential in biological studies that remains unexploited. Spectrally resolved FLIM (λFLIM) enables autofluorescence imaging with high image contrast that can be applied, for instance, in histopathology, particularly in the cancer field [8, 9]. Furthermore, spectral unmixing combined with lifetime sensing can probe multiple biochemical reactions and maximize the biochemical resolving power of a microscope [10–13].

However, FLIM, and λFLIM in particular, are not widely employed amongst the biomedical community because of the sophisticated technologies typically required to achieve spectrally resolved lifetime imaging, the limited acquisition speed and dynamic range, and the complexity of data interpretation. Spectral FLIM relies on the use of multi-anode photomultiplier tubes (PMTs) and fast electronics that build histograms of photon arrival times. Commercial systems route color information and share a single time-to-analogue converter (TAC) for time-correlated single photon counting (TCSPC) [14]. Such systems have been successfully used in biological applications (see [15] for a short description of several publications) and represent the gold standard in the field. However, multiplexing different spectral channels (*e.g.*, 16) over a single shared TAC exacerbates the limitations imposed by pulse pile-up on TCSPC in the presence of high (burst or constant) count rates. Although pulse pile-up can be more generally ameliorated by channel multiplexing, it remains an important limitation [16, 17]. Fereidouni and colleagues [12] have recently shown the feasibility of the integration of fast electronics at each anode of a multi-anode PMT, thereby achieving (using 7 anodes of a 32 multi-anode PMT) speed improvements limited only by the detector dead-time. However, this approach is limited by the small number of multi-anode

#243323 Received 18 Jun 2015; revised 5 Aug 2015; accepted 5 Aug 2015; published 28 Aug 2015

PMTs compatible with time-resolved imaging and the costs associated in scaling up the electronics for a fully integrated system.

To overcome these limitations, we [18, 19] and others [20] have developed linear sensors using complementary metal oxide semiconductor (CMOS) technology that integrate fast counting electronics within each pixel showing that these sensor architectures can achieve spectrally resolved lifetime sensing for micro-spectroscopy. Here, we demonstrate that the integration of a simple streamlined spectrograph with field-programmable gate array (FPGA) programming designed for efficient acquisition of images, and fast and efficient data analysis algorithms [21–24] together enables imaging applications with CMOS sensors equipped with fully parallel in-pixel photon-counting [18]. Exploiting these advances, we show how a compact, easy to interface and cost-effective system can achieve spectrally- and time-resolved imaging of typical samples with biological and medical significance.

2. Materials and methods

2.1 Microscopy

Fluorescence microscopy was undertaken with a bespoke two-photon laser-scanning microscope built with a Leica SP5 (Leica Microsystems UK Ltd) and equipped with a Ti:Sapphire laser (Chameleon Vision 2 by Coherent UK Ltd). A pulse-picker (pulseSelect by Angewandte Physik & Elektronik GmbH) was coupled to the Ti:Sapphire laser in order to reduce the repetition rate of the excitation source when necessary. Fluorescence emitted from the sample was directed to external detectors through the "X1 port" of the Leica SP5, collimated by an achromatic doublet of 100mm focal length and delivered to the sensor with a pair of silver coated mirrors as shown in Fig. 1(a). After the collimating lens, a custom-built motorized turning mirror was operated to deliver fluorescence emission onto the SPAD sensor or onto a commercial multi-wavelength FLIM (equipped with a multi-alkali PML-16C-1) operated by a SP150 electronic board (both from Becker & Hickl GmbH). A simple and compact direct vision spectrograph was built with a direct vision prism (G331120322 by LINOS Photonics GmbH) and an achromatic doublet of 25mm focal length to focus dispersed light onto the linear SPAD array. This focal length was selected to obtain appropriate spectral bandwidths (see section 2.5) and to underfill the transversal direction of the array (~50µm at full width at half maximum for a SPAD array width of 104µm) with the aim to minimize optical losses and simplify alignment. The camera lens was mounted on a z-axis translation mount and the SPAD array was mounted on a precision XYZ translation mount enabling fine alignment of the SPAD array with the prism. All the optics and the optomechanics were purchased from Thorlabs GmbH and Newport Spectra-Physics Ltd and had high efficiency anti-reflection coatings. All images were acquired with 256x256 pixels image format.

2.2 SPAD array

The sensor is an array (1.66mm x 104µm) of 64x4 single-photon avalanche diodes (SPADs) built using 0.35µm CMOS technology as previously described [18]. The four SPADs in the vertical direction are all connected to one read-out channel, improving effective detector dead-times (~50ns per channel) on a comparatively large sensitive area (15.8x63.2µm^2). Histograms of photon-arrival times are formed by four gated counters that are sequentially activated to enable in-pixel fluorescence lifetime sensing as shown in Fig. 1(b) [18, 25].

Digital delay lines for the control of the initial delay and the width of the four time gates were implemented on the same chip. With this prototype, the position and widths of the gates can be set with a resolution of ~1ns over a range of ~10ns. The position of the first gate relative to the laser pulse is further refined during calibration down to a resolution of 2.5ps with the use of the external delay line. As previously described [18], the instrument response function of each pixel is less than 160ps at full width at half maximum. The IRF and the positioning of the gates are fairly constant across the linear array (σ = 20ps) guaranteeing no

#243323 Received 18 Jun 2015; revised 5 Aug 2015; accepted 5 Aug 2015; published 28 Aug 2015

wavelength dependent bias in the measured lifetimes. It is important to notice that contrary to time-gating in wide-field imaging applications, time-gating in scanning systems is implemented without the loss of any photon [26]. Furthermore, gate widths can be optimized in order to maximize the photon economy of the detection and, therefore, the fluorescence lifetime resolving power [11, 25]. For this work, we followed indications described by Gerritsen *et al*. [25].

For the imaging applications described in this work, it was fundamental to develop a read-out sequence that would guarantee fast parallel read-out of the SPAD array synchronously to the laser clock and the microscope pixel trigger. These trigger signals provide the synchronization that enables the successful histogramming of fluorescence decays and image reconstruction. The acquisition protocol was executed by a FPGA. This architecture delivers a high dynamic range with counters of moderate dimension (8 bits) and minimizes, at the same time, losses that may occur during read-out. This system indeed counts photons seamlessly during image acquisition, whilst the FPGA accumulate the overall counts and coordinate the read-out of the SPAD array.

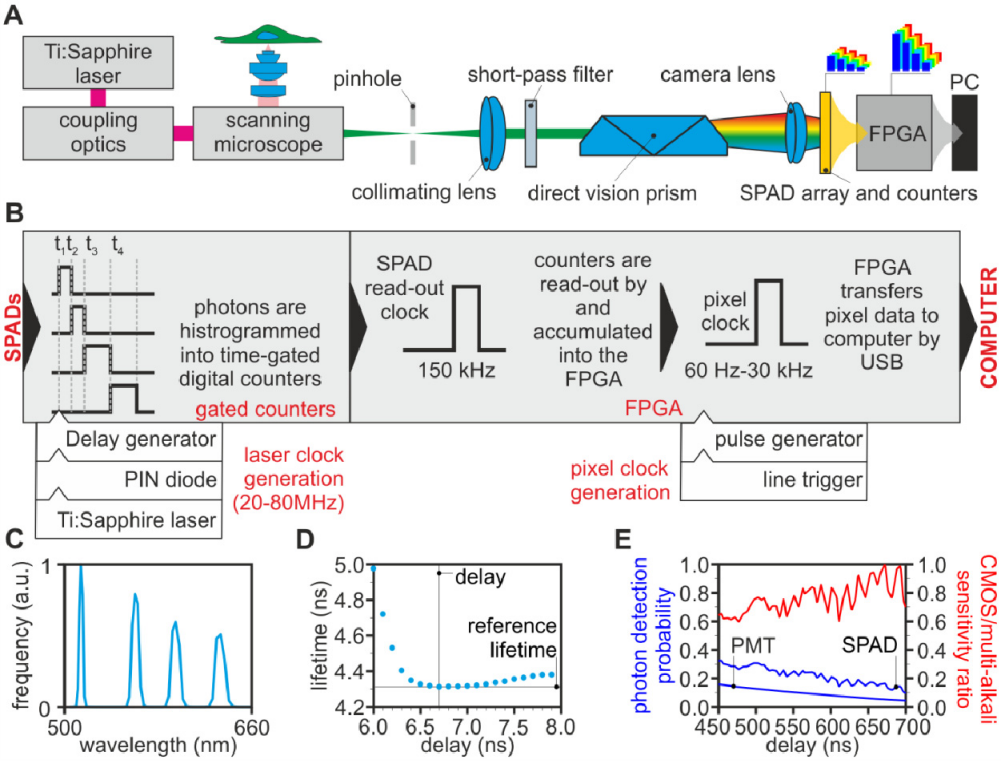

Fig. 1. System diagram: (a) The design of the λFLIM system, comprising a Ti:Sapphire laser, coupling optics, a laser scanning confocal microscope and a simple direct vision spectrograph based on the linear array of SPADs. (b) Diagram representing the read-out protocol of the SPAD array. A field-programmable gate array (FPGA) handles the complex sequence of triggers to provide a data stream to the computer via a standard USB connection. (c) Example of the laser comb (514-561-564-633nm) used for a spectral calibration. (d) Fluorescence lifetime estimation of the green plastic slide used as a reference for time calibration; the vertical and horizontal lines mark the delay and the minimum lifetime estimates, respectively. (e) Comparison of photon detection probability (blue curves) between a multi-alkali PMT photocathode and a SPAD built in CMOS technology and relative sensitivity ratio (red curves) obtained by dividing the CMOS to the PMT sensitivity (values with maximum normalized to one).

#243323 Received 18 Jun 2015; revised 5 Aug 2015; accepted 5 Aug 2015; published 28 Aug 2015

2.3 Read-out protocol

In order to handle large data streams from the sensor and to synchronize detection with image pixel acquisition and laser pulse, the sensor was installed in a fully integrated electronic board equipped with a XEM3050 FPGA (Opal Kelly Inc.). The board provides inputs for laser trigger and pixel clock signals. The pixel clock provided by the Leica SP5 Trigger Unit was not suitable for the operation of the sensor. Therefore, the line clock from the Trigger Unit was connected to a pulse generator TTI TG5011 (Thurlby Thandar Instruments Ltd) used to re-generate a suitable pixel clock within 60Hz-30kHz range depending on configuration. The trigger signal provided by the Chameleon laser is very noisy and it is not always reliable for direct triggering of other devices. Therefore, synchronization of the laser pulses with the sensor was achieved by monitoring the pulses after the pulse picker with the use of a beam sampler (Newport) and a fast PIN diode (Thorlabs). The signal was fed to a digital delay generator (DEL-350 by Becker&Hickl) that was used to trigger the sensor with 20ns broad pulses. The external delay generator and signal generators can be either not used with other lasers or confocal systems, or can be integrated on-board in future SPAD-based sensors. It should be noted that the Leica SP5 exhibits an uneven pixel dwell time because of the uneven speed of the scanners utilized by Leica also during the section of the field of view used for imaging; by regenerating the pixel clock, we employed a constant pixel dwell time. Figure 1(b) illustrates the key elements of the read-out protocol: i) a laser clock enables the first time-gated counter; ii) on-chip (FPGA-programmed) timers sequentially enable the following counters in user-defined time windows; iii) each detected photon is counted in the respective in-pixel time-gated counter; iv) the FPGA reads all accumulated photon counts at a SPAD array frame-clock (1-150kHz) and accumulates them in its internal memory; v) the pixel clock triggers the FPGA to transfer data to a computer through a USB connection. Particular care was employed in order to buffer SPAD array frame clock and confocal pixel clock when the FPGA was busy during data transfer in order to assign SPAD array data-frames unambiguously to the individual pixels of the confocal image.

2.4 Sample preparation

Stained and mounted sections of *Convallaria majalis* were purchased from Leica. HeLa cells were plated out into 4-well chambers (LabTek chambered coverslips) at a seeding density of 40,000 cells per cm^2. Cells were transfected with mAmetrine fused to tdTomato (plasmid 18879 from AddGene) [27] or mAmetrine alone (cloned from the former construct) with Effectene accordingly to the supplier's protocol. 48 hours after transfection, cells were washed with PBS, fixed with 4% paraformaldehyde and kept in PBS for imaging. Explanted organs were fixed in formalin solution (10% neutral-buffered) for 24hrs before transfer to 70% ethanol storage. Tissues were embedded in paraffin and 5µm sections cut and mounted onto poly-lysine coated slides. Before label-free tissue imaging slides were deparaffinised and rehydrated according to standard protocols. Briefly slides were washed twice with Xylene (10 minutes per wash) followed by a sequential ethanol gradient of 100%, 95%, 80%, 70% ethanol (5 minutes incubation per wash). Finally, slides were dipped into water and dried before imaging.

2.5 Calibration

Spectral calibration was performed by measuring the internal reflection onto the objective lens of a laser comb generated by the typical laser lines available by the Leica SP5 (*e.g.*, 458nm, 488nm, 514nm, 561nm, 594nm, and 633nm depending on the spectral bandwidth sampled in individual experiments). Spectral FLIM images were summed over the time and spatial dimensions to generate a measured spectrum corresponding to the known laser lines as shown in Fig. 1(c). After interpolation onto a ten times finer wavelength grid, this spectrum was fitted with multiple Gaussians and the estimates of the central wavelength of each

#243323 Received 18 Jun 2015; revised 5 Aug 2015; accepted 5 Aug 2015; published 28 Aug 2015

Gaussian *versus* pixel number were used to define the central wavelength of each spectral channel. This correspondence between spectral channel and absolute wavelength (reference laser lines) was then interpolated to obtain reference values for each SPAD/PMT element by fitting a polynomial of the first degree (for the PMT/TCSPC system) or the second degree (for the SPAD-based system) to model the dispersion of the grating and the prism, respectively. Spectral lines had a typical image on the linear array corresponding to a maximum of 2 SPAD elements at full width at half maximum along the direction of the array. The spectral bandwidth of the spectrograph depends on the wavelength projected onto the detector because of the non-linear dispersion of the prism: ~80nm over the blue-green range (<520nm) and >150nm in the red range. Accordingly, spectral resolutions of a few nanometers were achieved over the 450-650nm range. The range of detected wavelengths was tuned accordingly to individual experiments simply translating the SPAD array in front of the prism and camera lens by means of a precision translation stage.

In time-gated lifetime imaging, routinely performed with a lower number of time gates compared to TCSPC, it is crucial to position the first time-gate just after the rising time of the fluorescence decay. If one of the time gates capture the rising time, fluorescence lifetime estimations obtained by fitting data with an exponential decay will be incorrect. On the other hand, if the first time-gate is triggered too long after the laser excitation pulse, significant photon losses will result in a poor signal-to-noise ratio. Therefore, time-gated systems require day-to-day time calibration. The estimation of the delay between the laser pulse and the opening of the first time-gate can be obtained by imaging at varying delay times a reflection of the light source, a second harmonic signal or fluorescence emitted by fluorophores with a very short lifetime (*e.g.*, Rose Bengal). However, excitation and emission wavelengths of these references [28] are often difficult to match to those used in experiments in a two-photon spectrally resolved detection system. Therefore, we typically use fluorescent plastics to generate a reference lifetime signal. Figure 1(d) shows the effect of different delay times on fluorescence lifetime estimations of a green plastic slide (Chroma Technology). We have used these curves to estimate the delay to apply to the first gate, by estimating the point at which the fluorescence lifetime fit converged to a minimum value. The digital delay line DEL-350 offered a delay resolution of 2.5ps.

Furthermore, data analysis algorithm required knowledge of the widths of the time gates. Assuming that background noise is time independent, the width of each time gate relative to the first gate was estimated by measuring how many dark counts were collected in each gate during an image acquisition performed with the closed shutter in the emission path. The time width of the first gate was then fixed to match the fluorescence lifetime estimates with the known fluorescence lifetime value of the reference sample. The calibration of time gate widths was not required on a day-to-day basis. The estimate of the uncorrelated background described here was also used for background subtraction whenever explicitly declared in the text.

2.6 Data analysis

Data analysis of data collected with the SPAD system was performed with bespoke software written in Matlab (Mathworks). RGB representations were obtained by summing photon counts within three spectral ranges: lower than 495nm, 495-570nm and greater than 570nm for blue, green and red, respectively. In order to provide an optimal contrast with the samples of *Convallaria majalis* and fluorescent proteins, the boundary for the red channel was set at 619nm (the wavelength of the local minimum between two spectral peaks) and 545nm (the wavelength at which tdTomato emission is larger than mAmetrine), respectively.

Lifetime images were obtained by summing all spectral channels within each pixel and fitting a single exponential curve by nonlinear regression. TCSPC data was analysed with SPCImage v3.5 (Becker&Hickl). A bi-dimensional convolution averaging filter with 3x3 kernel was applied and pixels with very low photon counts were masked.

#243323 Received 18 Jun 2015; revised 5 Aug 2015; accepted 5 Aug 2015; published 28 Aug 2015

In order to detect the second harmonic signal shown in Figs. 4(h)-4(n), the first time gate was calibrated to overlap in time with the laser pulse; only the following three time gates were used for the fit-based estimation of fluorescence lifetimes shown in Fig. 4(j). However, the second harmonic signal is shown in all other panels and used also in the phasor-based unmixing.

Because of an uneven pixel dwell time exhibited by the Leica SP5 confocal microscope, images exhibit uneven brightness or uneven pixel resolution along the fast scanning axis depending on the choice of operation of the detector. We opted to use an even pixel dwell time; therefore, all SPAD-based images were processed with spatial interpolation along the fast scanning axis in order to compensate spatial deformation and to provide an adequate comparison with TCSPC data. On the other hand, TCSPC data were corrected for uneven pixel dwell time by multiplying the actual photon counts by a spatially dependent scale factor (larger than or equal to one). These corrections permitted us to generate images as if the Leica SP5 had a constant pixel dwell time and thus to provide an accurate comparison between TCSPC and SPAD data. Furthermore, the direct vision prism used in the spectrograph exhibit nonlinear dispersion and, therefore, a spectral flat field correction was applied to take into account differences relative to the multi-wavelength TCSPC where a grating was used as a (linear) dispersive element. Data was presented without any further correction to permit a direct comparison between the data generated by the two systems. However, the nominal sensitivity of the SPAD/CMOS technology [29] and the PMT/multi-alkali photocathode [30] are shown in Fig. 1(e) to enable a better interpretation of the data presented in Fig. 2.

"Phasor plots" have been generated by transforming the data with discreet cosine and discreet sine transforms as already described elsewhere [3, 12, 13, 21–23, 31]. Time and spectral phasors of the pure components were calculated by blind unmixing as described by Fereidouni *et al.* [31]. This method does not require any *a priori* knowledge about fluorophores thus providing a fast (~1-2 seconds on a standard computer) and model-free analysis of complex data sets. Shortly, low intensity pixels were masked, pixel-wise time-, spectral- and time-spectral- phasors were computed for all the remaining pixels as described by Eqs. (4), 5 and 6 of [31]. Spectral and time phasors of the pure components were calculated by fitting four planes to the linear combination of time, spectral and time-spectral phasors (Eqs. (24) and 25 in [31]) using total least square or QR decomposition algorithms and subsequently solving system of the four equations (Eqs. (29) and 30 in [31]). This step of phasor-based computation was performed on the images binned 4x4 in the spatial dimensions in order to obtain very high signal-to-noise ratios. All subsequent unmixing steps were performed on the original data. Fractional intensities of each pure component at every pixel were calculated using Eqs. (32), 33 and 34 in [31]. It should be noted that Eqs. (31) in [31] contains typographical errors; the correct system of equations that we solved numerically is:

$$v_x^D A_{kx}^2 + (u_x^D - v_x^{AD} + A_{kx} w_x^D) A_{kx} - u_x^{AD} - A_{ky} w_x^{AD} = 0 \tag{1}$$

$$w_y^D A_{ky}^2 + (u_y^D - w_y^{AD} + A_{kx} v_y^D) A_{ky} - u_y^{AD} - A_{kx} w_y^{AD} = 0 \tag{2}$$

Furthermore, we needed to adapt the time phasors to the use of time gates of uneven width. At low gate numbers, FLIM experiences degradation in signal-to-noise ratio [25, 32] and the locus of single exponential decays is not a semi-circle [21, 24] but a rotated arch [22]. In order to avoid this loss of precision and to maximize biochemical resolution, time gates of uneven width were used [11]. The resulting arch is profoundly altered by this procedure, but linearity of the representation is preserved therefore allowing the use of the same formalism for blind unmixing that is briefly described. However, for visualization purposes we computed the resulting arch numerically and fixed the origin of the arch to the origin of the Cartesian space by applying a simple rigid translation to the phasor plots.

#243323 Received 18 Jun 2015; revised 5 Aug 2015; accepted 5 Aug 2015; published 28 Aug 2015

3. Results

3.1 Fast and simple spectral FLIM with high dynamic range

To exemplify the capabilities of this novel detection system, images of *Convallaria majalis* were acquired at the excitation wavelength of 840nm and compared to images obtained with a commercial multi-wavelength TCSPC system. TCSPC images were acquired with an 80MHz laser repetition rate maximizing its acquisition speed, while the SPAD array was operated at a lower laser repetition rate (20MHz) where the current implementation of the electronics is more efficient.

Figures 2(a)-2(c) show the data set that we first collected with the spectrally resolved TCSPC operated at its maximum count-rate set to avoid pulse pile-up for an acquisition time of 360 seconds resulting in the detection of a maximum ~4,000 photons in the brightest pixels. We then attempted to acquire the same number of photons on the same field of view with the SPAD array as shown in Figs. 2(d)-2(f). The solid-state spectral FLIM was capable to obtain a similar image with similar photon counts (~4,000) with a higher number of spectral channels (64 *vs* 16) and in just 8.5 seconds, therefore resulting in a net increase of acquisition speed in excess of one order of magnitude despite the fact that the TCSPC system was operated at 4 times higher laser repetition rate. Acquisition speed is, however, not the only important outcome resulting from the reduction of sources of pulse pile-up and the parallelization of the spectral detection. The possibility to sustain high count rates also permits us to collect images with high dynamic range. Figures 2(g)-2(i) exemplify this feature, with images that we acquired with the SPAD array using a 1 minute acquisition time. This time we obtained maximum counts per pixel of ~18,000 photons therefore allowing to acquire images with dimmer areas exhibiting excellent photon counts (>1,000) and with brighter regions that did not cause saturation of the detectors.

The true colour images displayed in Figs. 2(b), 2(h) and 2(i) are computed over the data sets by discarding fluorescence lifetime information (*i.e.*, summing photons over the time dimension) as described in [33]. Spatially averaged fluorescence spectra are shown in Fig. 2(k) where similar spectral features are collected by the two different instruments. The relative weight of the two peaks and the absence of a tail at higher wavelengths for the SPAD-based measurements correlate with the different spectral-dependent sensitivity of the detectors as shown in Fig. 1(e) and differences in optical transmission of the spectrographs (*e.g.*, the commercial TCSPC-based system uses a grating that exhibits lower sensitivities at higher wavelengths, not shown). The bandwidth of the spectrographs is also different (see section 2.6); for the experiment shown in Fig. 2, it was set to 500-700nm for TCSPC and 510-680nm for the SPADs. Furthermore, small ripples in the green component of the spectra are visible for the SPAD-based detection because of the typical sensitivity profiles of CMOS technologies [29].

Figures 2(c), 2(f) and 2(i) show fluorescence lifetime images that were computed summing photons over the spectral dimension and Fig. 2(j) shows the respective spatially averaged histograms. Pulse pile-up would result in apparent shorter lifetimes at high count rates. However, the overall spectral and lifetime images and distributions are similar between TCSPC and SPADs. This demonstrates that despite the very high count rates reached by the SPAD arrays relative to spectral TCSPC (~720kHz for TCSPC, *i.e.* ~1/10 of the laser repetition rate set at 80MHz and ~27MHz for SPADs, *i.e.* 1.35 times the repetition rate set at 20MHz), data generated by the SPAD array does not exhibit pulse pile-up. Therefore, small discrepancies in the distributions of fluorescence lifetimes can be attributed to differences in spectral sensitivities (lifetime components at distinct spectral regions will be weighted differently), decay fitting algorithms. TCSPC and time-gating, when using a different number of gate will also exhibit differences in accuracy and precision in particular for shorter lifetime values [25, 32], differences that can be ameliorated by optimized gating profiles [11, 25].

#243323 Received 18 Jun 2015; revised 5 Aug 2015; accepted 5 Aug 2015; published 28 Aug 2015

Time-resolved emission spectra (TRES) [34] are shown in Fig. 2(l) and 2(m) exemplifying how spectra evolve in time. The main differences in the TRES measured with the SPAD array and TCSPC are the spectral resolution (higher with the SPAD array), the sampling resolution of the decays (higher with TCSPC electronics) and the already described differences in spectral sensitivity of each detector. TRES measured with the SPAD array may appear faster because of the different sampling resolution, but they are indeed similar as shown in Figs. 2(c), 2(f), 2(i) and 2(j).

The good quality of the images collected with the SPAD array and the histograms of lifetime and spectra shown in Figs. 2(j)-2(m) demonstrates the overall good performance of this prototype system and its capability to deliver measurements at count rates at least ~40 times higher than commercial TCSPC electronics for spectral FLIM.

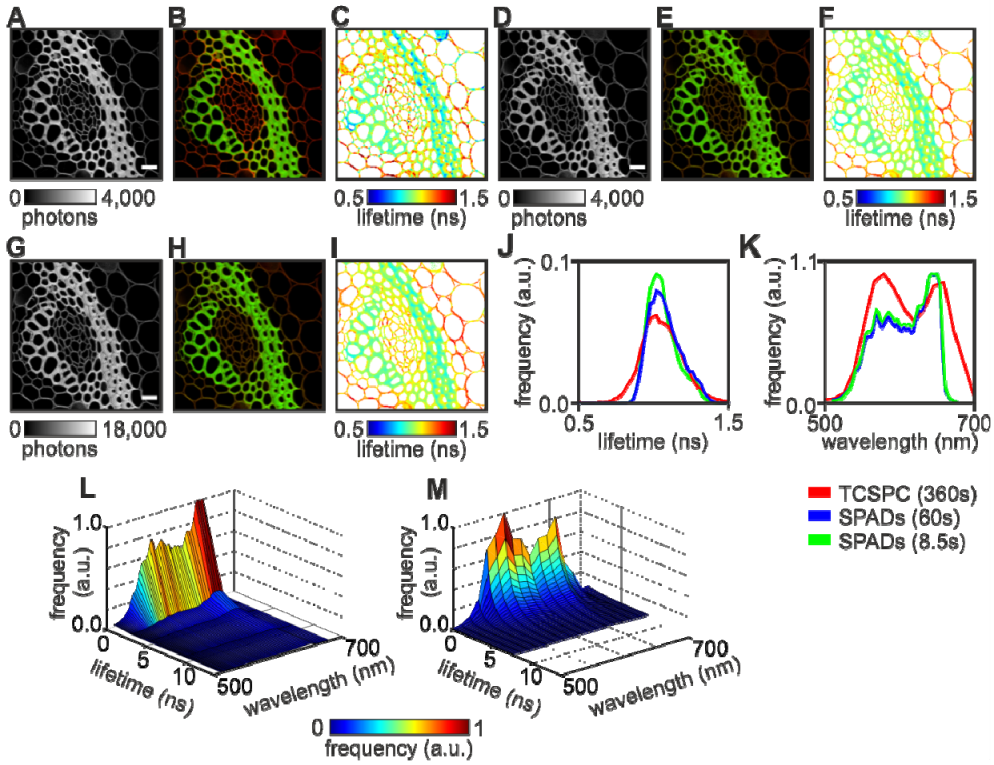

Fig. 2. Fast acquisition speed and high dynamic range. Photon counts (a, d and g), colour (b, e and h) and fluorescence lifetime images (c, f and i) of the reference sample *Convallaria majalis* measured by a PMT-based system in 360 seconds (a-c) and the SPAD-based system in ~8 seconds (d-f) or in ~1 minute (g-i) acquisition time. Laser power was adjusted to maximize count rates for each instrument and condition (1-1.5mW to obtain higher count rates for the SPAD-based measurements and ~300µW to avoid pulse pile-up in TCSPC). (j) Histograms of the estimated fluorescence lifetimes (histogram area normalized to one) and (k) emission spectra (each curve normalized to their maximum) for each of the images shown. Time-resolved emission spectra measured with SPADs or TCSPC are shown in panel (l) and (m), respectively. Scale bar: 20µm.

3.2 Simple and efficient data analysis

We have highlighted differences in spectral and time-resolved features in the fluorescence emission detected by different instruments. However, the analysis of biologically relevant samples is often performed with model-free analysis tools nowadays. This allows neglecting the fine spectroscopic features of fluorescence emission that depends on several instrumental and environmental factors and, at the same time, retrieving important biological estimates

#243323 Received 18 Jun 2015; revised 5 Aug 2015; accepted 5 Aug 2015; published 28 Aug 2015

such as relative concentrations or enzymatic activities with fast algorithms and minimal user input. For instance, spectral- and time- phasors for the representation and analysis of λFLIM data have been proposed [11, 31, 35]. Phasors have been also used to simplify blind unmixing of unknown species [31]. Figure 3 illustrates the performance of this technique adapted and applied to data collected with our solid-sate detector (see Section 2.6). This method enables the unmixing of up to three components; inspection of phasor plots shown in Figs. 3(a)-3(c) reveals the presence of three clouds of pixels corresponding to uncorrelated noise (dark counts, N) and two fluorophores which relative unmixed intensities are shown in magenta (M) and green (G) in Fig. 3(d). The reference semi-circle representing the locus of single exponentials [21, 22] is shown in gray in Fig. 3(a). However, the small number of time-gates [22] and their uneven width selected to maximize signal-to-noise ratios [11, 25] alter the shape and position of the reference semi-circle. The reference arch is therefore computed numerically for lifetimes in the range of 0ns to 100μs with the gate width values of 2/2/4/4 nanoseconds (see Section 2.2 and Gerritsen *et al.* [25] for details on the selection of time gate widths) used for the acquisition; this arch is shown in black in Fig. 3(a) (see Section 2.6 for details). Importantly, the uneven width of the gates preserved the linearity of time-phasors. The reference circle for spectral phasors depends on the number of spectral detection channels, and the phasor position depends on the central wavelength of the spectra and its width [12, 23, 31]. Here we show the reference circle centered at the origin with a radius equal to one just for visualization purposes. Figure 3(d) demonstrates the high contrast that this microscopy system can provide together with this phasor-based blind unmixing algorithm. Here we show the relative intensities of the two fluorophores (in magenta and green) that have been used to stain *C. majalis*.

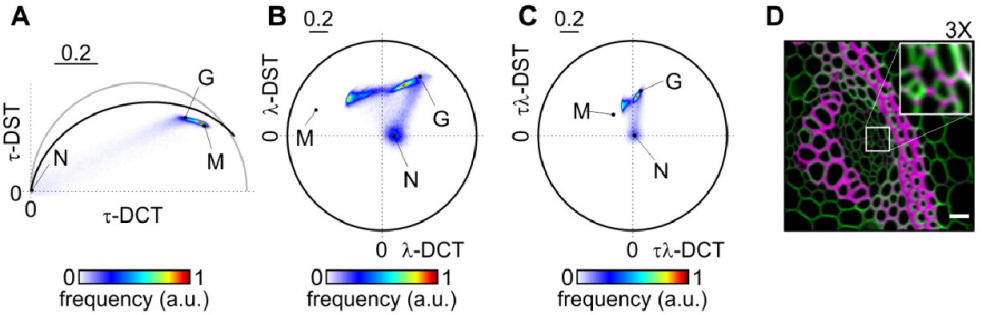

Fig. 3. Simple and efficient blind unmixing. Decay curves represented with phasor plots by discrete sine and cosine transforms (DST and DCT) in time (τ, panel (a)), spectral dimension (λ, panel (b)) and two-dimensional transforms (τλ, panel (c)) enables the identification of populations of fluorophores without any *a priori* information. (d) Relative intensities of the two fluorophores used to stain the sample shown in Figs. 2(g)-2(i) obtained by global analysis of phasor-transformed data and blind unmixing. Dots and letters in panels (a-c) indicate the unmixed phasors of noise (N, not shown in panel (d)), and two fluorophores represented in magenta (M) and green (G). The insert in panel (d) shows a 3x magnification of the image to display the level of separation achieved with this technique (brightness and contrast adjusted for best display).

3.3 Medical imaging

An important emerging application of hyperspectral and lifetime sensing is label-free tissue imaging [8, 36]. A simple time-resolved spectrograph for either imaging (this work) or spectroscopy applications [20] may be extremely useful for fluorescence-guided biopsies, surgery and label-free histopathology. We tested this potential application by imaging an unstained section of metastatic pancreatic ductal adenocarcinoma in liver tissue excised from a tumorigenic murine model [37]. Images were acquired with autofluorescence excited at 840nm as shown in Figs. 4(a)-4(g) or 920nm in Figs. 4(h)-4(n), and emission collected over

#243323 Received 18 Jun 2015; revised 5 Aug 2015; accepted 5 Aug 2015; published 28 Aug 2015

the 450-530nm spectral range. A second harmonic signal is also present when the sample is excited at 920nm resulting in a narrow (see section 2.6 for details) blue emission typical of collagen as shown in Fig. 4(i). Figure 4 demonstrates that novel solid-state technologies and pixel designs are already able to acquire (within 4 minutes) colour and lifetime images of high quality.

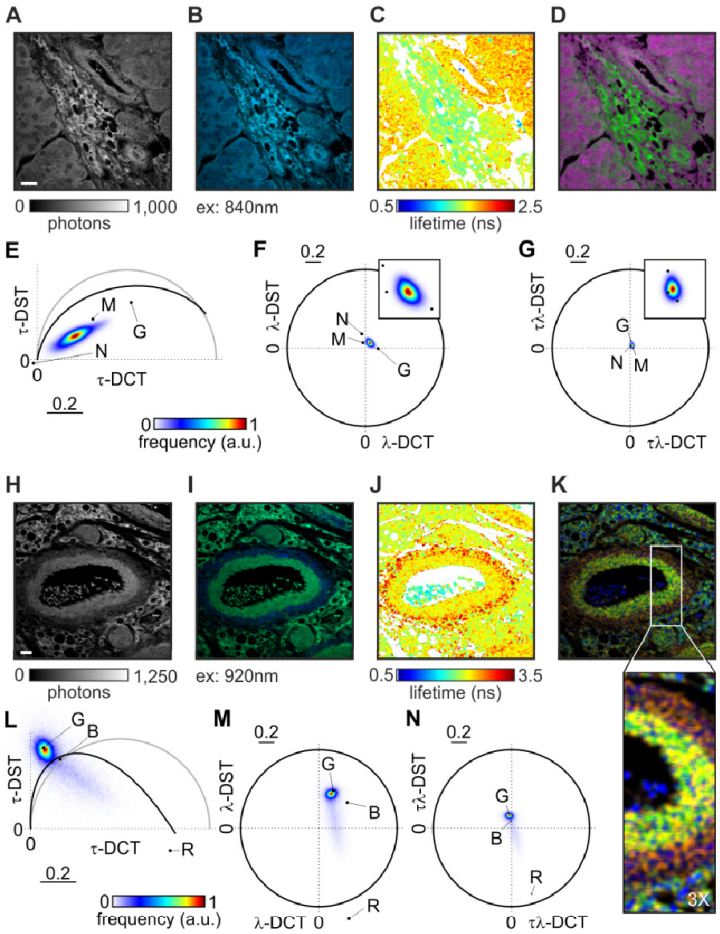

Fig. 4. Label-free tissue imaging. Photon counts (a, h), true-colour (b, i) and fluorescence lifetime (c, j) images of unstained liver tissue excised from a tumorogenic murine model. Images in the top row were measured with excitation at 840nm. The other images were acquired with excitation at 920nm, with the first time-gate used to detect the second harmonic signal generated by collagen (blue color in (i)). Blind unmixing performed with the use of phasors (e-g, l-n) exhibits maximum image contrast within a single image; panels (d) and (k) show the fractional intensities of the unmixed components. A region in panel (k) is shown with a 3X magnification to illustrate the level of separation between different regions that this technique can achieve (brightness and contrast adjusted for best display). The letters in the phasor plots mark the pure unmixed phasors of noise (N), and fluorophores which fractional intensities are displayed in blue (B), green (G), red (corresponding to a dominant second harmonic signal, R) and magenta (M) in panels (d) and (k). Scale bar: 20μm.

Phasor-based blind unmixing was able to separate different tissue environments successfully. Figures 4(a)-4(g) show that tissue autofluorescence did not exhibit a large contrast when excited at 840nm (gates of 2/2/4/4ns width); phasor analysis on the original data revealed the presence of two spectrally similar but yet distinct optical signatures which relative unmixed intensities are depicted in Fig. 4(d) in magenta and green. The presence of

#243323 Received 18 Jun 2015; revised 5 Aug 2015; accepted 5 Aug 2015; published 28 Aug 2015

these two environments was evident also from the inspection of lifetime data, but phasor analysis can separate the contribution of those two signatures to the total fluorescence of the sample in a quantitative manner. Like in the example demonstrated in Fig. 3, the third component is uncorrelated noise (N), therefore enabling simple denoising of the image. Figures 4(h)-4(n) show that tissue autofluorescence exhibited a more complex signature when excited at 920nm (gates of 1/2/2/4ns width) also for the presence of a strong second harmonic signal as shown by the blue emission in Fig. 4(i) and the correspondent unmixed signals (in red) in Fig. 4(k). Therefore, uncorrelated noise had to be removed prior to phasor analysis by subtraction of background (see section 2.5). Blind unmixing of denoised data results in the separation of the three fluorescent signals which relative intensities are shown in Fig. 4(k) in blue (B), green (G) and red (R). These correspond to the *tunica media* (inner side, yellow) and *tunica externa* (outer side, red) of a blood vessel containing red blood cells (blue) in the lumen.

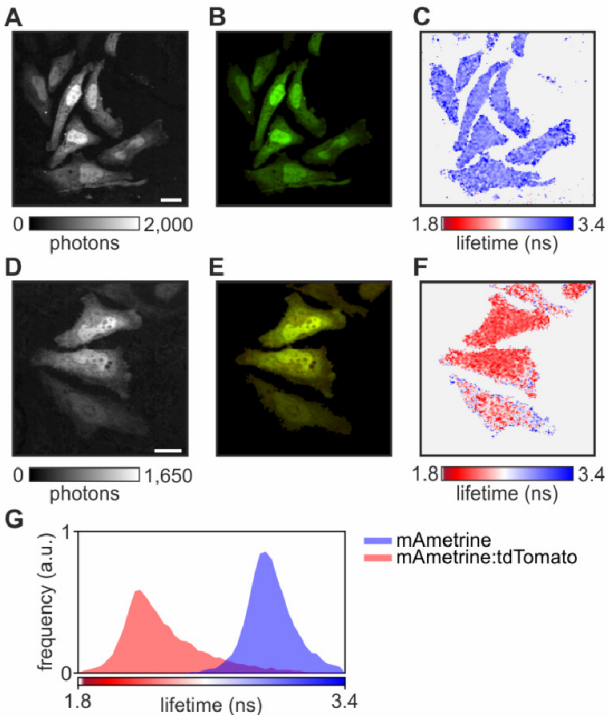

Fig. 5. Biochemical imaging. HeLa cells expressing the fluorescent protein mAmetrine (a-c) and the fusion construct of mAmetrine and tdTomato (d-f) exhibiting ~30% FRET efficiency. Photon counts (a, d), true colour images (b, e) and fluorescence lifetime images (c, f) are shown. The histogram of the estimated fluorescence lifetimes is shown in panel (g). Scale bar: 20µm.

3.4 Biochemical imaging in living cells

Whereas an analysis of how to achieve separation of biochemical reactions is beyond the scope of this work, we tested the sensor performance in detecting FRET on living cells expressing fluorescent proteins in order to provide additional reference data to understand the performance of the system. Figures 5(a)-5(b) show the brightness and true-colour images of HeLa cells expressing the long Stokes-shifted fluorescent protein mAmetrine [27] excited at 840nm. Photon counts (1,500-2,000) were sufficient to obtain fluorescence lifetime images in 4 minutes as shown in Fig. 5(c). Figures 5(d)-5(f) show images of HeLa cells expressing a fusion of mAmetrine and tdTomato. These linked fluorescent proteins undergo Förster

#243323 Received 18 Jun 2015; revised 5 Aug 2015; accepted 5 Aug 2015; published 28 Aug 2015

resonance energy transfer (FRET), a process widely used in biology to sense protein-protein interactions or post-translational modifications of proteins [38]. Figures 5(b) and 5(e) show the shift in colour of the sample caused by tdTomato sensitized emission and Figs. 5(c) and 5(f) show the FRET-dependent decrease (~30%) of mAmetrine fluorescence lifetime (images of mAmetrine were computed over the spectral range of 511-545nm). The histograms of fluorescence lifetimes are also shown in Fig. 5(g) for comparison. Figure 5 demonstrates the sensor can generate high quality time- and spectrally- resolved images of living cells for biochemical imaging.

4. Discussion

We have aimed to demonstrate that CMOS technologies for time-resolved sensing of fluorescence are sufficiently mature to be successfully integrated into microscopy systems capable of performing complex assays and imaging challenging samples of biomedical relevance. However, SPAD arrays of this complexity are prototypes and exhibit limitations such as a comparatively low sensitivity caused by sub-optimal quantum efficiency (32% at λ = 450nm), fill factor (34%), dark counts (1kHz/SPAD) and low time-gates number that are typical of test systems [18]. Nevertheless, even with the current prototype, we have shown that a simple spectrograph built with an array of SPADs integrating in-pixel time-gating can already generate high resolution images of representative fluorescent samples such as mammalian cells expressing fluorescent proteins and tissue autofluorescence. Also, we have shown that the full parallelization of the photon detection and time gating enables complex image acquisitions at unprecedented speeds (~8s versus 360s of the commercial system). Therefore, even marginal improvements of our technology could routinely provide hyperspectral and lifetime images of biological samples at the same speed as a standard confocal microscope. For instance, minor improvements on board electronics can enable repetition rates of 80MHz potentially resulting in a 4-fold increase in speed and fill factors may be improved through use of microlens arrays from ~30% to ~90% [39]. Quantum efficiencies could be also increased from 30% to 60% by improved optical stack (*e.g.*, thinning, special anti-reflecting coating layers, light-pipe structures) and optimized doping profiles. Furthermore, the dark counts rate can be dramatically decreased from 1kHz/SPAD to less than 10Hz with optimized and full custom development of the SPAD within the standard CMOS fabrication flow, improved substrate quality and process, gettering, optimized doping profile and cooling [40].

Spectral FLIM is notoriously slow and the demonstration of this faster technology is important to foster applications for live cell imaging and micro-endoscopy where acquisition times may be critical. However, we envisage that the high dynamic range offered by these integrated systems is equally (or even more) important because acquisition speed is often limited by the brightest pixels in an image. The number of spectral channels is often not a critical parameter in biomedical applications. Over the last decade, however, multi-spectral and hyperspectral (*e.g.*, with 32 spectral channels) confocal microscopes became the gold standard at the high-end of readily available commercial systems. This is because of their flexibility (no filters), optical efficiency (<20% losses) and enhanced capabilities (*e.g.*, spectral unmixing) in the life sciences. In addition to this, a higher number of spectral channels is desirable for all applications wherein spectra are unknown, for example, in tumor imaging. SPAD arrays in CMOS technology can be extended to larger formats and number of gates expanding to virtually unlimited count rates (640MHz in this work compared to 5MHz for commercial systems), very high spectral and time resolutions with limited increase of costs, something impossible with photo-multiplier tubes. For these reasons, we believe that CMOS detectors carry a high unexploited potential for laser scanning microscopy, in particular for spectrally and time resolved applications that we have demonstrated in this work.

#243323 Received 18 Jun 2015; revised 5 Aug 2015; accepted 5 Aug 2015; published 28 Aug 2015

The strength of our approach is the careful integration of streamlined dispersive optics, with FPGA programming for the lossless detection of photon streams at high rates, and the in-pixel time-gating. Together, these result in a very efficient and compact system that extend to imaging (as shown here) powerful capabilities that have been demonstrated only recently for spectroscopic applications [19, 20]. The concomitant improvement of performance and simplification of spectral FLIM elegantly blend with the availability of recent techniques for model-free, fast and simple analysis of spectral- and time- resolved data. We have adapted phasor analysis techniques [21, 24, 41] to the study of time-gated [22] spectrally resolved images with gating schemes adapted to optimize the signal-to-noise ratio [11, 25] and demonstrated fast and successful blind unmixing of tissue autofluorescence. We have also shown images of living cells expressing fluorescent proteins undergoing FRET as a proof-of-concept for biochemical imaging. Therefore, we envisage that spectral FLIM will enable the multiplexing of multiple FRET pairs, a technically challenging technique that is still under development in a several laboratories [11, 27, 42–45].

Spectral FLIM and its applications to biochemical and medical imaging will remain challenging applications compared to more traditional assays (*e.g.*, Western-blotting, immuno-precipitation and immuno-histopathology); however, with such a simple, compact, USB-connected camera system and data analyses that combine the power of intuitive graphical representations with sophisticated quantitative interpretation that does not require user intervention, technical hurdles to the effective use of spectral fluorescence lifetime imaging may be considered practically eliminated.

Taken together with recent progress in the field [18, 20, 46–51], the data we report in this work demonstrate the potential for a major transition in detector technologies available for applications in the biosciences. Arrays of CMOS pixels together with novel data processing methodologies will soon enable complex photonic solutions to be applied to routine assays in the non-specialist laboratory. With the growing interest in solid-state pixels that integrate computational power (in-pixel histogramming in this work) for fluorescence detection, we foresee a new era for time-resolved applications including routine quantitative biochemical and medical imaging.

Acknowledgments

A.E. thanks the EPSRC for the initial funding of the project (EP/F044011/1) from 2009 to 2011. M.P. and L.D.C. were supported by a Programme Grant to A.R.V. from the UK Medical Research Council (MRC). This project was also supported by the MRC's grant-in-aid to the Cancer Unit, Cambridge (A.E., A.R.V.). C.F.K acknowledges funding from the MRC (grant MR/K015850/1), the Wellcome Trust (grant 089703/Z/09/Z) and the EPSRC (EP/L015889/1). We would like also to thank Dr. Farzad Fereidouni (UC Davis Medical Center) for discussion and support on the phasor-based blind unmixing of images and Mr. Maximilian Fries (MRC Cancer Unit) for the subcloning of mAmetrine.